IEEE Access
Multidisciplinary ⋮ Rapid Review ⋮ Open Access Journal

Received 16 May 2024, accepted 30 May 2024, date of publication 4 June 2024, date of current version 12 June 2024.

Digital Object Identifier 10.1109/ACCESS.2024.3409454

RESEARCH ARTICLE

Numerical Prediction of the Effect of Typical Particle Properties on a Centrifugal Pump

YINGYU JI[1], JIANGBO TONG[2], YULIANG ZHANG[1], XIAOWEI XU[1], YANJUAN ZHAO[3], AND JINSHUN ZHU[4]

[1]College of Mechanical Engineering, Quzhou University, Quzhou 324000, China
[2]School of Mechanical Engineering, Hunan University of Technology, Zhuzhou 412007, China
[3]College of Information Engineering, Quzhou College of Technology, Quzhou 324000, China
[4]Visu Autotech (Ningbo) Company Ltd., Ningbo 315191, China

Corresponding author: Yuliang Zhang (zhang002@sina.com)

This work was supported in part by the Science and Technology Project of Quzhou under Grant 2023K256 and Grant 2022K98, and in part by Zhejiang Provincial Natural Science Foundation of China under Grant LZY21E050001.

ABSTRACT To grasp the hydraulic performance and abrasion characteristics of a particular model pump before manufacture, this paper firstly numerically calculates the three-dimensional viscous steady incompressible flow of a solid-liquid two-phase flow centrifugal pump with specific speed $n_s = 93$ based on the Mixture model and obtains the influences of the three typical particle attributes (particle diameter, solid-phase concentration, and solid-phase density) on the hydraulic performance of the calculation model pump. Subsequently, numerical prediction of the abrasion of major overflow parts due to particle collision impacts was carried out based on the DPM model. The results show that the solid-phase concentration has the most significant effect on the hydraulic performance of solid-liquid two-phase flow pumps, and the diameter of solid-phase particles has the most minor effect. With the increase of particle diameter and solid-phase concentration, head and efficiency are gradually reduced. In contrast, with the increase of solid-phase density, head and efficiency show a trend of increasing and decreasing. The most severe decrease in hydraulic performance occurs at a C_v of 30%, where the head decreases to 20.19m, and the efficiency decreases to 66.90%. With the increase of the three typical solid-phase properties, the abrasion in the overflow inner wall surface of the solid-liquid two-phase flow centrifugal pump shows different degrees of deterioration, and the maximum degree of wear of about 0.0010kg/m^{2}s.

INDEX TERMS Centrifugal pump, solid-liquid two-phase flow, particle property, performance prediction, abrasion.

I. INTRODUCTION

Centrifugal pumps play an important role in petrochemistry, agricultural irrigation, aerospace, biomedicine, and other fields [1], [2], [3], [4], [5], [6]. Most centrifugal pumps are designed by the clear water pump, when the transport medium contains solid particles, due to the complex flow pattern in the pump and the uncertainty of the shape, size, and concentration of the solid particles, the performance will undoubtedly appear to change. At present, CFD technology has been widely used in pump research [7], [8], [9], [10], which is of great significance in reducing manufacturing costs and shortening the development cycle. With the help of CFD technology and experimental tests, scholars have carried out extensive research on solid-liquid pumps.

For the hydraulic performance and internal flow characteristics under solid-liquid mixing, Wang et al. investigated the effect of particle concentration and particle size on the performance of a double-suction centrifugal pump. They found that the head of the centrifugal pump decreases with increasing particle concentration and particle size [11]. Rahul et al. studied a centrifugal slurry pump and found that the performance of the centrifugal pump is inversely proportional to the increase in particle size and concentration [12]. Wang et al. simulated two-phase flow in a centrifugal pump using the Mixture model [13]. It was found

The associate editor coordinating the review of this manuscript and approving it for publication was Lei Wang.

that with the increase in particle size and volume concentration, the pressure inside the flow field decreases, and the external characteristic curve shows a decreasing trend. Li et al. conducted numerical simulations and performance tests for a solid-liquid centrifugal pump at different solid particle diameters and two-phase mixture concentrations [14]. At low flow rates, the variation of solid-phase parameters has a minimal effect on the performance. Zhang et al. simulated the solid-liquid two-phase flow in a low specific speed centrifugal pump [15]. It was found that the increase in particle size and concentration reduces the pump's hydraulic performance, the effect of particle density on the performance is relatively small, and the tailing structure around the tongue is more evident at high concentrations. Liu et al. studied the two-phase flow of a sewage pump under different operating conditions and particle sizes. They found that the distribution of solid particles in the impeller channel is mainly related to the particle size, with big particles mainly retained in the vicinity of the impeller hub and intermediate impeller channel and small particles mainly retained in the vicinity near the hub and the impeller inlet [16]. Wang et al. investigated solid-liquid two-phase flow inside a deep-sea mining pump and revealed that the intensity and size of the vortex inside the guide vanes increase significantly, and the change in the flow velocity is more evident when the particle size increases [17]. Zhao et al. numerically investigated the transient characteristics of sand-containing two-phase flow in a centrifugal pump. They found that higher particle concentrations improve the hydraulic performance and turbulent kinetic energy of the centrifugal pump and that changes in particle diameter have a relatively small effect on the transient flow of the centrifugal pump [18].

Due to the solid impurity particles in the conveying medium, there is a general abrasion of the overflow parts of the pump, which leads to a decline in the pump's performance and the reduction of operating life. For the wear and tear problem of pumps when conveying mixed solid-liquid media, Wang et al. investigated the effect of particle shape, particle concentration, and particle size variation on the wear of different overflow wall surfaces in a centrifugal pump. It was found that the larger the particle shape sphericity, the smaller the wear area of the blades' pressure surface [19]. Li et al. used the CFD-DEM method to simulate the transport of large particles in a centrifugal pump and found that the instantaneous wear rate of the impeller, volute, and wear plate varied periodically with the rotation of the impeller; the wear rate increased with the increase of the particle mass concentration [20]. Hong and Hu conducted a numerical calculation of wear and a wear test study on a deep-sea mining pump. They found that the test wear area matched the numerically calculated wear area [21]. In addition, under low flow conditions, the distribution of wear on the surface of the primary impeller is more decentralized than that of the secondary impeller. When the flow rate increases to the design flow rate, the wear on the impeller and guide vane surfaces is distributed in bands, and the wear pattern is more regular. At the same time, Hong et al. studied the wear of different components within a deep-sea mining pump under different particle sizes, particle volume concentrations, particle densities, and different flow rates and rotational speeds [22]. It was found that the larger the particle size, the higher the particle density, and the higher the flow rate, the greater the average wear rate, where the higher the particle density, the more concentrated the severe wear area. Peng et al. investigated solid-liquid two-phase flow in a heavy-duty slurry pump at different particle concentrations and flow rates [23]. The results showed that the pump's flow resistance, backflow, and local wall wear increased with the increase in particle concentration. Liu et al. numerically simulated an oilfield electric submersible pump using the discrete phase model DPM and found that the wear rate increased with increasing sand concentration and pump speed [24]. The particle size has a more significant effect on the impeller wear, which increases and then decreases with the increase in particle size. Khalid et al. designed and fabricated a wear test rig to conduct wear experiments on the pump and found that the wear in the middle region of the impeller was more severe than the wear in the edge region [25]. Zhao et al. used a numerical model combining computational fluid dynamics [26], [27], [28] and the discrete element method (DEM) to simulate the erosion inside the centrifugal pump. They found that the erosion and wear are more severe in the inlet and outlet of the pressure side of the impeller blade, the middle of the blades, and the vicinity of the tongue [29].

In conclusion, a wealth of research has been carried out by different scholars on the hydraulic performance and abrasion prediction of different types of pumps when conveying solid-liquid mixtures in different application environments. However, their research results are all based on their different specific objects, and there are apparent differences between different objects when conveying different solid-liquid media. The authors of this paper propose to design and manufacture a centrifugal pump with a low specific speed of $n_s = 93$, which also faces the problem of decreased performance and wear of the overflow parts when conveying solid-liquid two-phase fluid flow before being put into practical application. With the help of the CFD method, under different solid-phase particle diameters, solid-phase volume fractions, and solid-phase densities, this paper predicts the hydraulic performance based on the Mixture model, and also explores the mechanism of energy loss in the pump by using entropy production theory, and then predicts the wall abrasion based on the DPM model and the Finnie wear model, expecting to grasp the effect of the typical particles on the hydraulic performance and abrasion characteristics of this centrifugal pump, and providing improvement basis and direction for enhancing the pump and finalizing manufacture.

II. CALCULATION MODEL AND METHOD

A. PHYSICAL MODEL

The calculated model is a solid-liquid two-phase centrifugal pump with specific speed $n_s = 93$, which is designed with

flow rate of 25m^3/h, head of 20m and speed of 2900r/min. The main geometric parameters are shown in Table 1.

TABLE 1. Main geometric parameters.

Parameters	Value	Parameters	Value
Inlet diameter D_s	65mm	Inlet placement angle β_1	25°
Outlet diameter D_d	50mm	Outlet placement angle β_2	20°
Number of blades Z	6	Blade wrap angle φ	120°
Impeller diameter D_2	137mm	Impeller outlet width b_2	10mm

B. CONTROL EQUATION

According to the Navier-Stokes equations [30], [31] and considering the interphase coupling between the solid and liquid phases, the momentum equations for the solid and liquid phases are established separately. If the solid-phase volume concentration in the two-phase flow is denoted by C_V, then the volume of the liquid-phase in any two-phase flow with volume Vm is $(1-C_V)V_m$. The liquid-phase momentum equation is

$$\frac{d\vec{u}}{dt} = \vec{F}_f - \frac{1}{\rho_f}\nabla p + \nu\nabla^2\vec{u} + \frac{\vec{F}_{fs}}{\rho_f(1-C_V)} \tag{1}$$

The solid-phase momentum equation is

$$(1 + C_\xi\frac{\rho_J}{\rho_s})\frac{d\vec{u}_s}{dt} - C_\xi\frac{\rho_f}{\rho_s}\frac{d\vec{u}}{dt} = \vec{F}_s - \frac{1}{\rho_s}\nabla p + \frac{\vec{F}_{fs}}{\rho_s C_V} \tag{2}$$

The continuity equations for the solid and liquid phases are

$$\frac{\partial(\rho_s C_V)}{\partial t} + \nabla\cdot(\rho_s C_V\vec{u}_s) = 0 \tag{3}$$

$$\frac{\partial\left[\rho_f(1-C_V)\right]}{\partial t} + \nabla\cdot\left[\rho_f(1-C_V)\vec{u}_f\right] = 0 \tag{4}$$

The solid-liquid two-phase flow interphase coupling equation is

$$\vec{F}_{sf} = -\vec{F}_{fs} \tag{5}$$

The Mixture multiphase flow model [32] is a continuous-phase computational model, that can simulate solid-liquid two-phase flow by calculating the motion equations of the mixed phase and obtaining information about the velocity and pressure, etc., of the liquid and solid phases in the flow field. In this paper, the Mixture multiphase flow model is used to simulate the solid-liquid two-phase flow in the pump to obtain the internal and external characteristic changes caused by the change of particle properties. The continuity equation describing the solid-liquid two-phase flow is

$$\nabla\cdot(\rho_m v_m) = 0 \tag{6}$$

The momentum equation is

$$\nabla\cdot(\rho_m v_m v_m) = -\nabla_p + \nabla\cdot[\mu_m(\nabla v_m + \nabla v_m^T)] + \rho_m g + F + \nabla\cdot(\sum_{k=1}^{n}\alpha_k\rho_k v_{dr,k}v_{dr,k}) \tag{7}$$

where ρ_m is the mixing density, kg/m^3; μ_m is the mixing viscosity coefficient, Pa· s; F is the volume force, N; v is the mass-averaged velocity, m/s; n is the number of phases; α_k is the volume fraction of the kth phase; ρ_k is the density of the kth phase, kg/m3; $v_{dr,k}$ is the drift velocity of the kth phase, m/s. The drift velocity v_{dp} is the velocity of the solid phase relative to the liquid phase

$$v_{qp} = v_p - v_q \tag{8}$$

Therefore, the relationship between drift velocity and slip velocity is

$$v_{dr,k} = v_{qp} - \sum_{k=1}^{n}\frac{\alpha_k\rho_k}{\rho_m}v_{qk} \tag{9}$$

From the continuity equation of the solid phase, the volume fraction equation of the solid phase is given by

$$\nabla\cdot(\alpha_p\rho_p v_m) = -\nabla\cdot(\alpha_p\rho_p v_{dr,p}) \tag{10}$$

Meanwhile, the Lagrange Discrete Phase Model (DPM) [33] is used to simulate and calculate the solid-liquid two-phase flow in the centrifugal pump. The wall wear caused by solid-liquid flow is predicted by using the Finnie wear model [34], [35], which explains the wear law under polygonal abrasive grains and low impulse angle. The abrasion rate is,

$$ER = kV_p^n f(\gamma) \tag{11}$$

where

$$f(\gamma) = \begin{cases} \frac{1}{3}\cos^2\gamma & \tan\gamma > \frac{1}{3} \\ \sin(2\gamma) - 3\sin^2\gamma & \tan\gamma \le \frac{1}{3} \end{cases} \tag{12}$$

where V_P represents the velocity of particles colliding with the wall, m/s; $f(\gamma)$ is the particle impact angle function. The solid-phase particle impact angle is the angle made by the direction of particle motion tangential to the wall surface. The index n is determined by the nature of the material, and takes the value of 2.3 to 2.5 for commonly used metallic materials.

C. CALCULATION DOMAIN MESH

Fig. 1 shows the calculation domain and meshes of the solid-liquid pump. Secondary flow regions such as front and rear chambers are ignored in the modeling, the effect of secondary flow regions on pump performance is obtained by empirical correction. The calculation model is divided using unstructured meshes, and structured meshes are locally assisted divisions. Unstructured meshes are used for the impeller and volute shell sections, while structured meshes are generated for the inlet section. The quality of the meshes has been checked, and the meshes are all above 0.2. Fig. 2 shows the grid-independence test, which finalized the number of grids to 652,344. Meanwhile, the mesh near the wall was encrypted to ensure that the flow conditions in the boundary layer can be accurately captured and the y$^+$ value is guaranteed to be

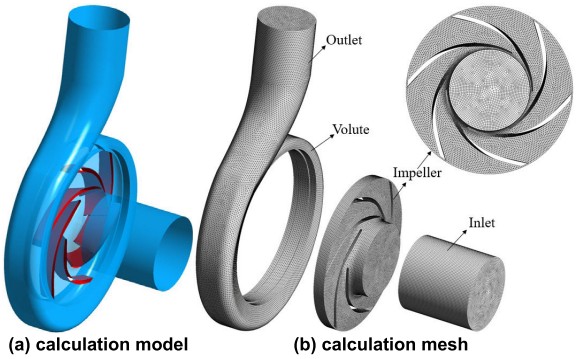

FIGURE 1. Calculation model and mesh for solid-liquid pump.

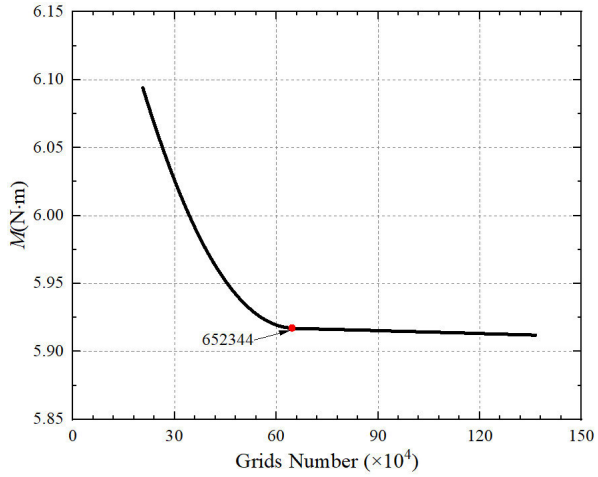

FIGURE 2. Grid independence verification.

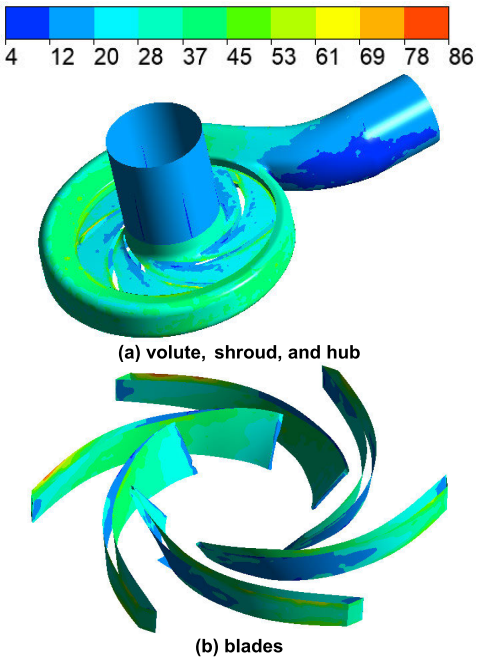

FIGURE 3. Contours of the y^+ distributions around walls.

within 100 [36], [37], [38], the y^+ value cloud of the wall is shown in Fig. 3.

D. CALCULATION SETTING

The velocity inlet is selected as the boundary condition in the inlet. Based on the conservation of mass and fluid's incompressibility, the axial velocity value at the inlet can be given according to the regulated flow rate and the size of the inlet piping, and assuming that the tangential and radial velocities are zero. The turbulent kinetic energy k and turbulent dissipation rate ε at the inlet can be determined by the following equation:

$$\begin{cases} k = \frac{3}{2}(I\bar{u})^2 \\ \varepsilon = C_\mu^{3/4}\frac{k^{3/2}}{l} \end{cases} \tag{13}$$

where $l = 0.07L$, and L is the characteristic length (the value taken in this paper is the diameter at the inlet). I is the turbulence intensity, $I \approx 0.16Re^{-1/8}$, $\mathrm{Re} = \frac{\bar{u}\cdot L}{\nu}$, $\bar{u}$ is the average velocity at the inlet. $C_\mu \approx 0.09$ is the empirical constant in the turbulence model.

In this paper, the free outflow boundary condition is selected and the flow at the outlet of the calculation domain is assumed to be fully developed, and the velocity component u_{out}, the pressure p_{out}, the turbulent kinetic energy k_{out}, and the turbulent dissipation rate ε_{out} take the second type of boundary conditions, i.e.

$$\frac{\partial u_j|_{out}}{\partial \vec{n}} = 0, \frac{\partial p_{out}}{\partial \vec{n}} = 0, \frac{\partial k_{out}}{\partial \vec{n}} = 0, \frac{\partial \varepsilon_{out}}{\partial \vec{n}} = 0 (j = 1, 2, 3) \tag{14}$$

Numerical calculation simulations are mainly used to set the conditions of different particle diameters, phase concentrations, and densities to study the effect of solid phase on the solid-liquid pump. The Mixture multiphase flow model and the RNG k-ε turbulence model are adopted to reveal the changes in internal and external properties caused by particle properties. The liquid phase is the incompressible fluid (clear water), which is set as the primary phase, and the solid phase is assumed to be the continuous medium (sand), which is set as the secondary phase. Considering the slip velocity between phases, the drag calculation adopts the Schiller-Naumann model, and the restitution coefficient is 0.9. The Lagrange Discrete Phase Model (DPM) and the Finnie wear model are used to predict the location and extent of abrasion due to solid-liquid flow. Set the inlet face of the computational domain as the particle incidence face, the particle incidence velocity is the same as the inlet velocity of the liquid phase, specify the incoming particle material as sand, ignore the influence of the particle shape on the calculation, and the default particle shape is a regular sphere. Set the inlet and outlet faces of the computational domain to be the free entry and exit faces of the particles, and set the rest of the walls to be the rebound walls.

E. CALCULATION METHOD

The actual volume flow rate of the pump is obtained by numerical integration of each mesh cell on the inlet or outlet

cross-section and is defined as

$$Q = \int_A (\vec{v} \cdot \vec{n}) dA \tag{15}$$

where A is the area of the cross-section at the inlet or outlet, $\vec{v}$ is the velocity vector of the mesh surface cell on the inlet or outlet cross-section, and $\vec{n}$ is the normal unit vector of the mesh surface cell at the inlet or outlet.

The total pressure at the inlet and outlet is described using the mass-weighted average and can be defined as

$$\bar{p}_r = \frac{\int_A (\rho p |\vec{v} \cdot \vec{n}|) dA}{\int_A (\rho |\vec{v} \cdot \vec{n}|) dA} \tag{16}$$

where p is the total pressure of the mesh surface cells on the inlet or outlet cross-section, and ρ is the density of the conveying fluid.

The head is defined as the energy increment from the inlet to the pump outlet, i.e., the difference in pressure head between the pump inlet and outlet plus the difference in position head (the effect of gravity is taken into account)

$$H = \left\{ \sum_{i=1}^{N} \left(\frac{P}{\rho g}\right)_i \Big/ N + \sum_{i=1}^{N} \left(\frac{V^2}{2g}\right)_i \Big/ N \right\}_{outlet} - \left\{ \sum_{i=1}^{M} \left(\frac{P}{\rho g}\right)_i \Big/ M + \sum_{i=1}^{M} \left(\frac{V^2}{2g}\right)_i \Big/ M \right\}_{inlet} + \Delta h \tag{17}$$

where P is the pressure value at the center of the mesh cell; V is the absolute velocity at the center of the mesh cell; ρg is the heaviness of the conveying fluid; M and N are the number of mesh cells on the inlet and outlet cross-section of the impeller. When the gravity is considered, Δh is the vertical distance from the pump outlet plane to the center axis of the inlet line, and g is the gravity acceleration.

The torque provided by the impeller is the resisting torque overcome when the impeller rotates to do work, defined as

$$M = \left(\int_S (\vec{r} \times (\vec{\tau} \cdot \vec{n})) dS\right) \cdot \vec{a} \tag{18}$$

where S is the surface area of all rotating parts, $\vec{\tau}$ is the total stress tensor, and $\vec{a}$ is the unit vector parallel to the axis of rotation.

The hydraulic efficiency is

$$\eta_h = \frac{\rho g Q H}{M \omega} \tag{19}$$

where Q is the flow rate, M is the impeller torque, and ω is the angle velocity.

The volume efficiency is

$$\eta_v = \frac{1}{1 + 0.68 n_s^{-2/3}} \tag{20}$$

The total efficiency is

$$\eta = \left(\frac{1}{\eta_v \eta_h} + \frac{\Delta P_d}{P_e} + 0.03\right)^{-1} \tag{21}$$

where P_e is the effective output power, $P_e = \rho g Q H$; ΔP_d is the disk friction loss, according to the following formula

a. When $n_s > 65$, $\Delta P_d = 1.1 \times 75 \times 10^{-6} \rho g u_2^3 D_2^2$

b. When $n_s < 65$, $\Delta P_d = 0.133 \times 10^{-3} \rho Re^{0.134} \omega^3 (D_2/2)^3 D_2^2$, where $Re = 10^6 \times \omega \times (D_2/2)^2$.

The initial values of the solid-phase medium are taken as density $\rho = 1500 kg/m^3$ with a particle diameter of 0.05mm and a concentration of 10%.

III. HYDRAULIC PERFORMANCE PREDICTION

A. NUMERICAL CALCULATION VALIDATION

The results of experiments and numerical predictions of the head, power, and efficiency of the centrifugal pump under clear water are compared to verify the accuracy of the simulation of centrifugal pump performance. As shown in Fig. 4, the numerical simulation results are consistent with the distribution of the experimental values, have the same trend of variation, and the relative error is within the acceptable range. As the flow rate increases, the head and power obtained from the test and numerical prediction increase gradually; the efficiency also increases and then decreases, reaching the maximum value near the flow rate of 29m^3/h. As can be seen, the trends of each external characteristic curve under numerical simulation and test are the same. It is also found that the head and power curves match well in the flow rate range from 10m^3/h to 32m^3/h, with a maximum error in the head of about 6.48% and a maximum error in power of about 5.51%. At all flow rates, the predicted efficiency is slightly higher than the experimental efficiency, with a maximum error in efficiency of about 10.13%. Under the rated flow rate of 25m^3/h, the test head, efficiency, and shaft power are about 21.05m, 67.41%, and 2.10kW, and the numerically predicted head, efficiency and shaft power are 21.71m, 74.24%, and 1.99kw, with relative errors of 3.14%, 10.13%, and 5.24%, and the deviations are all within a reasonable range, the overall match between the two is well. In conclusion, the

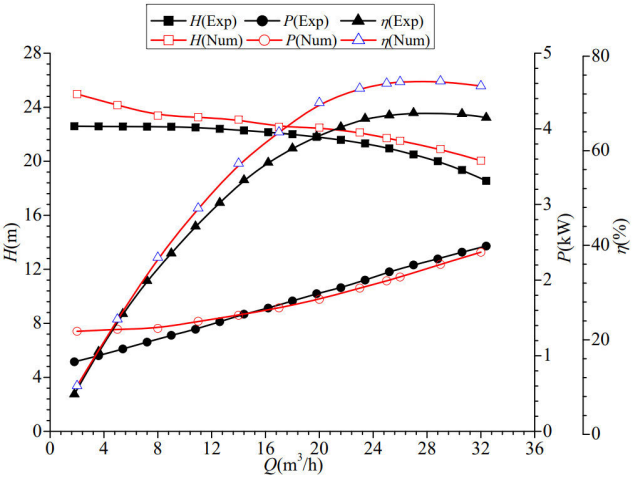

FIGURE 4. Comparison of external characterization results between experiments and numerical simulations.

calculation method is reliable, and the numerical results are accurate.

B. HYDRAULIC PERFORMANCE PREDICTION

The effect of solid-phase particle diameter on the pump's external characteristics is shown in Fig. 5. As can be seen, with the increase in the solid-phase particle diameter, the head of the solid-liquid pump subsequently decreases, and the conveying head decreases from the beginning of 20.70m to 20.51m, with a change value of 0.19m in the head, which is a relatively small degree of change. From the trend of efficiency change, when conveying solid-liquid two-phase flow, the conveying efficiency of the solid-liquid pump has a significant tendency to decrease, from 69.08% at the beginning to 68.79%. Under the same working conditions, the head and efficiency of solid-liquid pumps are reduced when conveying solid-liquid fluid relative to clear-water media. At d_s of 0.05mm, the reduction in head and efficiency is the least, with 1.02m and 5.16%, respectively; at d_s of 0.30mm, the reduction in head and efficiency is the most, with 1.21m and 5.45%, respectively. In summary, compared to clear water media, the head and efficiency of the centrifugal pump in conveying solid-liquid fluid are significantly lower, but the effect of particle diameter on the head and efficiency of the centrifugal pump in conveying solid-liquid fluid is small.

The variation of head and conveying efficiency of the solid-liquid pump under varying solid-phase volume fraction conditions is shown in Fig. 6. It is seen that the reduction in head and efficiency is less for low concentration conditions and more for high concentration conditions relative to clear water media. At C_v of 5%, the head is 20.90m, which is reduced by 0.81m and 3.73%. Moreover, at C_v of 30%, the head is 20.19m, which is reduced by 1.52m and 7%. It is also found that with the increase of solid-phase volume fraction, the head of the solid-liquid pump gradually decreases from the maximum value of 20.90m to the minimum head of 20.19m, which overall reduces the head by 0.71m; the conveying efficiency of the solid-liquid pump decreases from 71.49% to 66.90%, with an impact difference of 4.59%. The head and efficiency of the solid-liquid pump show a decreasing trend, and the effect of solid-phase concentration is more significant relative to the degree of influence of solid-phase particle diameter on the head and efficiency.

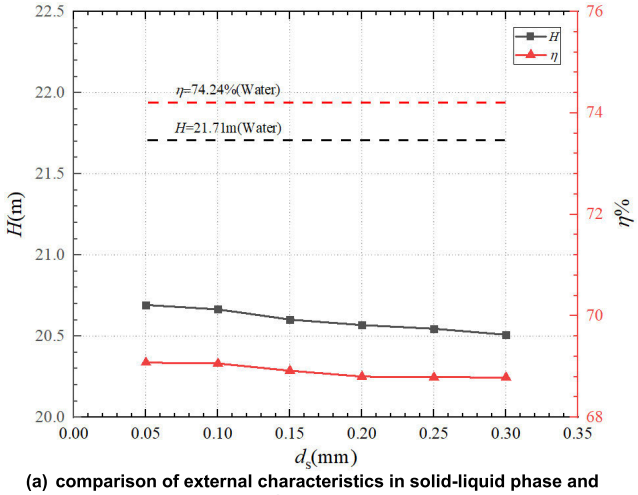

(a) comparison of external characteristics in solid-liquid phase and clear water

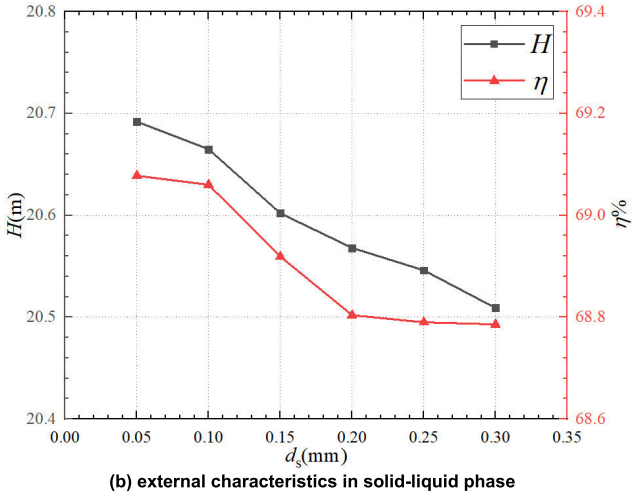

(b) external characteristics in solid-liquid phase

FIGURE 5. External characteristics at different particle diameters.

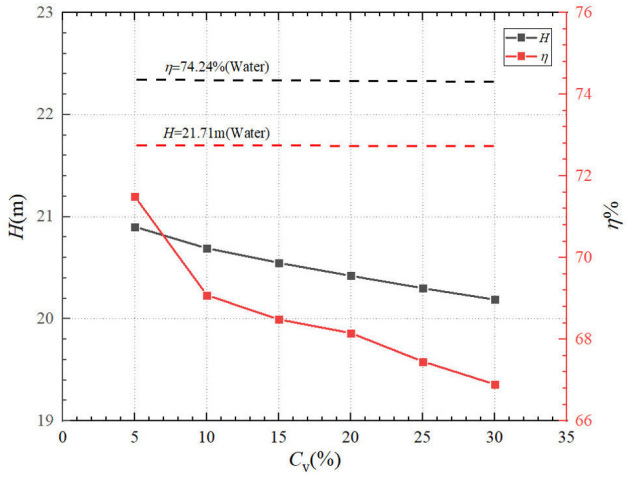

FIGURE 6. External properties at different solid-phase concentrations.

The head and efficiency variation curves of the solid-liquid pump under the effect of different solid-phase density conditions are shown in Fig. 7. It shows that the head and efficiency show a trend of increasing and then decreasing, and the solid-phase density has a significant effect on the external characteristics of the solid-liquid pump. When the solid-phase density increases from 500kg/m^3 to 1000kg/m^3, the head increases from 20.683m to 20.710m, and the efficiency increases from 68.960% to 69.118%, showing an increasing trend. Moreover, when the solid-phase density is higher than 1000kg/m^3, as the solid-phase density increases, the head starts to decrease gradually and finally to 20.529m, and the efficiency also decreases gradually to 68.372%. Compared to the first two solid-phase properties, it is concluded that the degree of influence of solid phase on the head and

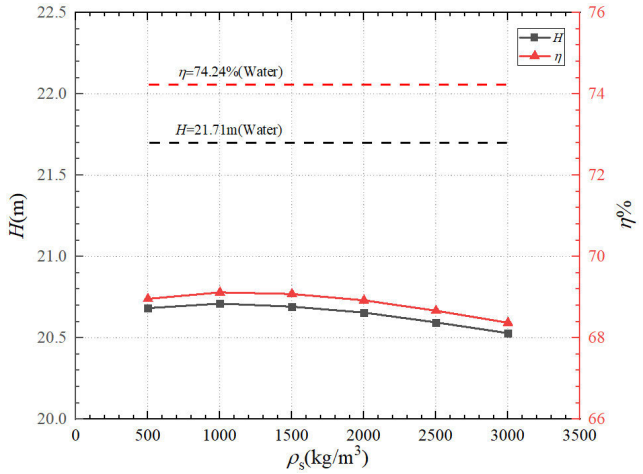

(a) comparison of external characteristics in solid-liquid phase and clear water

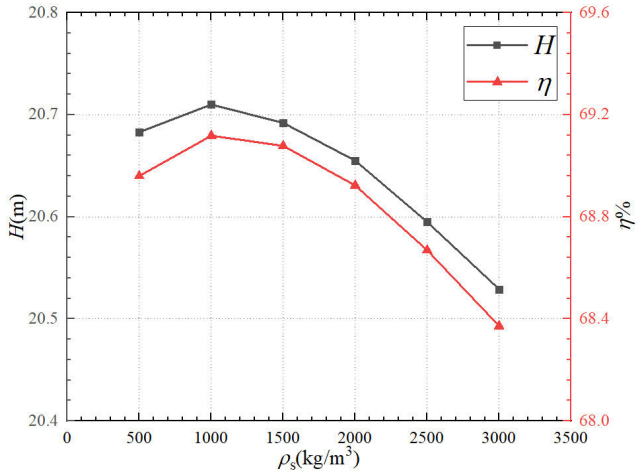

(b) external characteristics in solid-liquid phase

FIGURE 7. External properties at different solid-phase densities.

efficiency of solid-liquid pumps is as follows: solid-phase volume fraction > solid-phase density > solid-phase particle diameter.

Meanwhile, to explore the energy loss mechanism inside the pump, the entropy production theory [39], [40], [41], [42] is used in this paper to show the region of high hydraulic loss in the internal flow field. For turbulent flow in centrifugal pumps, entropy production arises from time-averaged motion and transient velocity fluctuation. The entropy production rate $\dot{S}'''$ is

$$\dot{S}''' = \dot{S}_D''' + \dot{S}_{D'}''' \tag{22}$$

$$\dot{S}_D''' = \frac{2\mu}{T}\left[\left(\frac{\partial \bar{u}}{\partial x}\right)^2 + \left(\frac{\partial \bar{v}}{\partial y}\right)^2 + \left(\frac{\partial \bar{w}}{\partial z}\right)^2\right] + \frac{\mu}{T}\left[\left(\frac{\partial \bar{v}}{\partial x} + \frac{\partial \bar{u}}{\partial y}\right)^2 + \left(\frac{\partial \bar{w}}{\partial x} + \frac{\partial \bar{u}}{\partial z}\right)^2 + \left(\frac{\partial \bar{v}}{\partial z} + \frac{\partial \bar{w}}{\partial y}\right)^2\right] \tag{23}$$

$$\dot{S}_{D'}''' = \frac{2\mu_{eff}}{T}\left[\left(\frac{\partial u'}{\partial x}\right)^2 + \left(\frac{\partial v'}{\partial y}\right)^2 + \left(\frac{\partial w'}{\partial z}\right)^2\right] + \frac{\mu_{eff}}{T}\left[\left(\frac{\partial v'}{\partial x} + \frac{\partial u'}{\partial y}\right)^2 + \left(\frac{\partial w'}{\partial x} + \frac{\partial u'}{\partial z}\right)^2 + \left(\frac{\partial v'}{\partial z} + \frac{\partial w'}{\partial y}\right)^2\right] \tag{24}$$

where: $\dot{S}_D'''$ is the velocity-averaged entropy production rate; $\dot{S}_{D'}'''$ is the velocity pulsation entropy production rate; μ is the kinematic viscosity; $\bar{u}$, $\bar{v}$, $\bar{w}$ are time-averaged velocity; u', v', w' is the pulsation velocity; T is the temperature, set to 293K; μ_{eff} is the valid kinematic viscosity, which is

$$\mu_{eff} = \mu + \mu_t \tag{25}$$

where μ_t is the turbulent kinematic viscosity.

In the SST k-ω turbulence model, the local entropy production due to velocity fluctuations $\dot{S}_{D''}'''$ [43] is

$$\dot{S}_{D''} = \alpha\frac{\rho\omega k}{T} \tag{26}$$

where $\alpha = 0.09$, ω is the turbulent vortex frequency, s^{-1}; k is the turbulence intensity, m^2/s^2

Since the entropy production rate has a strong wall effect and the time-averaged term is obvious, the entropy production near the wall $S_{pro,W}$ is

$$S_{pro,W} = \int_S \frac{\vec{\tau}\cdot\vec{v}}{T}dS \tag{27}$$

where τ is the wall shear stress, Pa; S is the area, m^2; v is the velocity near the wall, m/s.

The total entropy production in the computational domain of the whole system S_{pro} is

$$S_{\text{pro}} = \int_V \dot{S}_D'''dV + \int_V \dot{S}_{D'}'''dV + \int_S \frac{\vec{\tau}\cdot\vec{v}}{T}dS \tag{28}$$

The entropy production distribution for different solid phase properties is shown in Fig. 8. Overall, the entropy production is mainly distributed in the wall surface of the volute, the wall surface of the blades, and the junction region between the impeller and the volute, where the flow energy loss is greater. In addition, the wall region of the small warp angle of the volute is a high-entropy production region, and the energy loss is much larger than that of the wall region of the large wrap angle of the volute. At a particle diameter of 0.05 mm, the maximum entropy production value in the wall region of the small warp angle of the volute from the first section to the fifth section is about 1500 W/(m^3·K). In contrast, the entropy production value in the other wall regions of the volute is only about 900 W/(m^3·K). Relative to the wall region of the blades' pressure surface, the energy loss is greater in the wall region of the suction surface. As visible when the particle diameter is 0.05mm, the whole wall region of the suction surface is a high entropy production region, and the maximum

entropy production value is about 1500 W/(m^3·K); While in the wall region of the pressure surface, there is entropy production distribution only in the blade head, and the maximum entropy production value is only about 900 W/(m^3·K). It is also found that the entropy production value is higher at the blade tail, and the region of high entropy production is largest at the blade tail near the tongue. Compared with the entropy production distribution under different particle diameters, it is found that the difference in entropy production distribution is small, and the particle diameter has less influence on the entropy production distribution.

Compared with the entropy production distribution at different solid-phase concentrations, it is found that the entropy production distribution in the pump changes significantly with the increase of solid-phase concentration. At a solid-phase concentration of 10%, a high entropy production is generated only in the wall region of the volute range from the first to the fifth section, with a maximum entropy production value of about 1500 W/(m^3·K). As the solid-phase concentration increases to 20%, the high entropy production is distributed over almost the entire wall region of the volute, and the area of high entropy production distribution increases significantly. In addition, the distribution of entropy production in the region adjacent to the blade is significantly altered. For the pressure surface region of blades, the entropy production distribution range and entropy production maximum increase with increasing solid-phase concentration. Under low concentration conditions, the entropy production is mainly concentrated in the blade head region of the pressure surface, and the maximum entropy production value is about 900 W/(m^3·K). Moreover, under high concentration conditions, the entropy production distribution region extends from the blade head to the blade middle, and the maximum entropy production value is about 1500 W/(m^3·K). For the blade suction surface and tail region, the range of high entropy production distribution also increases with increasing solid-phase concentration. It is evident that the energy loss in the region near the blade is greater as the solid-phase concentration increases.

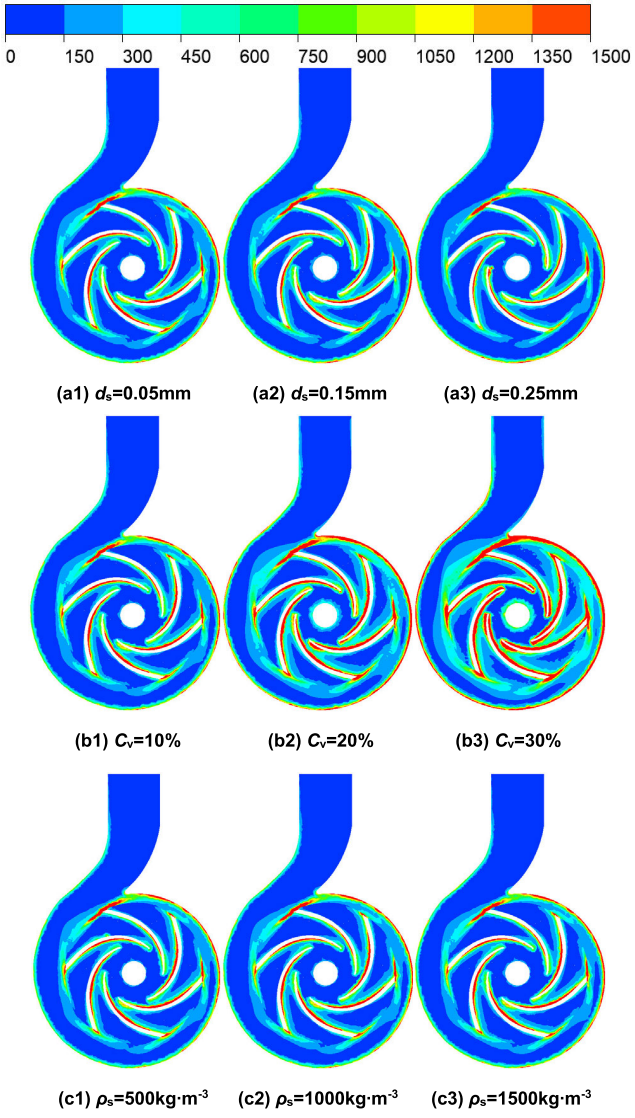

FIGURE 8. Distribution of entropy production with different solid phase properties (a1-a3: particle diameter; b1-b3: solid-phase concentration; c1-c3: particle density).

It is also found that the difference in the distribution of entropy production is small under different solid-phase densities. At different solid-phase densities, the entropy production is mainly distributed in the wall surface of the volute, the wall surface of the blades, and the junction region of the impeller and the volute, and the high entropy production region is also close to the same. It can be found that the change in solid-phase concentration has less influence on the entropy production distribution. In summary, the solid-phase volume fraction has the most significant effect on the entropy production distribution, while the solid-phase particle diameter and solid-phase density have a smaller effect on the entropy production distribution.

C. ABRASION PREDICTION

When the centrifugal pump conveys solid-liquid mixed media, the solid particles constantly collide with the internal wall of the pump overflow parts, and prolonged operation will lead to severe wear and tear inside the pump, affecting the normal operation performance and safety and stability of the centrifugal pump. Based on it, the influence of different solid-phase particle diameters, solid-phase densities, and solid-phase concentrations on the internal wear distribution characteristics of the centrifugal pump is investigated in this paper.

The wear clouds of the worm shell with different solid phase properties are shown in Fig. 9. As seen in the figure, the abrasion in the small wrap angle region of the volute is much more severe than that in the large wrap angle region of the volute, which agrees with the findings of Zhao et al. [44], [45]. At a particle diameter of 0.05 mm, the most severe wear region is the volute region from the first section to the second

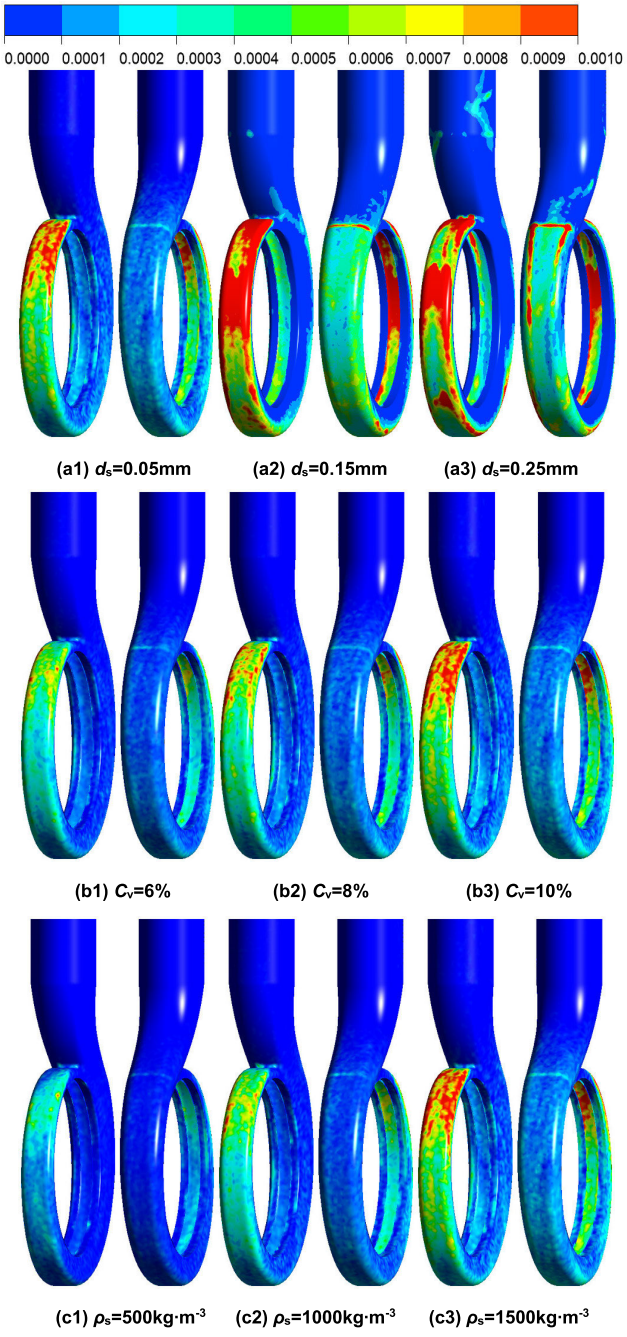

FIGURE 9. Abrasion distribution of the volute for different particle properties (a1-a3: particle diameter; b1-b3: solid-phase concentration; c1-c3: particle density).

section, with a maximum wear degree of 0.0010 kg/m^{2}s, and the other wall surfaces have a relatively light degree of wear. It was also found that the overall abrasion decreases gradually from the first section to the eighth section and then to the pump outlet. The volute from the first section to the second section is a severe abrasion region, with a maximum abrasion degree of 0.001kg/m^{2}s; the volute from the third section to the fifth section is a moderate abrasion region, with a maximum abrasion degree of about 0.0007kg/m^{2}s; the region from the fifth section to the pump outlet is a slight abrasion region, with a maximum abrasion degree of about 0.0003kg/m^{2}s. At a particle diameter of 0.15 mm, the range of severe abrasion region increases, expanding from the volute from the first section to the second section to the volute from the first section to the third section, with a maximum abrasion degree of about 0.0010 kg/m^{2}s. At the same time, significant abrasion also occurs in the big warp angle region of the volute, with a maximum abrasion degree of about 0.0007 kg/m^{2}s. Moreover, when the particle diameter increases to 0.25 mm, the abrasion in the volute's small and large warp angle regions also increases, and the entire tongue region also shows severe abrasion. In summary, the increase in particle diameter aggravates the abrasion in the tongue region and the small warp angle region of the volute, and the abrasion in the remaining spiral segments of the volute region also becomes significant with the increase in particle diameter, but is not as severe as that in the tongue region and the small warp angle region of the volute.

Fig. 9b$_1$-b$_3$ shows the wear cloud of the volute for different solid-phase concentrations. Overall, the abrasion in the volute region is mainly concentrated in the small wrap angle region of the volute, and the abrasion gradually decreases along the first section to the eighth section and then to the pump outlet. At a solid-phase concentration of 6%, the volute from the first section to the fifth section is mainly moderate abrasion, only a very small area is serious abrasion, and the serious abrasion area is sporadically distributed. At a solid-phase concentration of 8%, the volute from the first section to the second section shows a large area of serious abrasion, with a maximum abrasion degree of about 0.0010kg/m^{2}s; the volute from the second section to the fifth section is mainly moderate abrasion, with a maximum abrasion degree of about 0.0007kg/m^{2}s; and the abrasion in the other regions is very small. While at a solid-phase concentration of 10%, the abrasion in the volute from the first section to the second section is serious, with a maximum abrasion degree of about 0.0010 kg/m^{2}s; the abrasion in other regions is also more serious. Evidently, as the solid-phase concentration increases, the abrasion in the volute from the first section to the second section aggravates significantly, and large areas of serious abrasion appear.

Fig. 9c$_1$-c$_3$ shows the wear cloud of the volute for different solid-phase densities. At particle densities of 500 kg· m^{-3} and 1000 kg· m^{-3}, the abrasion is worse in the small warp angle region of the volute, while the abrasion on the other wall surfaces is lighter. As the particle density increases to 1500 kg· m^{-3}, the abrasion in the entire volute worsens, and it is most pronounced in the volute from the first section to the second section. Evidently, the abrasion in the small wrap angle region of the volute near the tongue is more serious as the solid-phase density increases. To sum up, with the increase of solid-phase particle diameter, solid-phase density, and solid-phase concentration, the abrasion in the volute gets more serious, and the abrasion in the volute from the first section to the second section worsens the most.

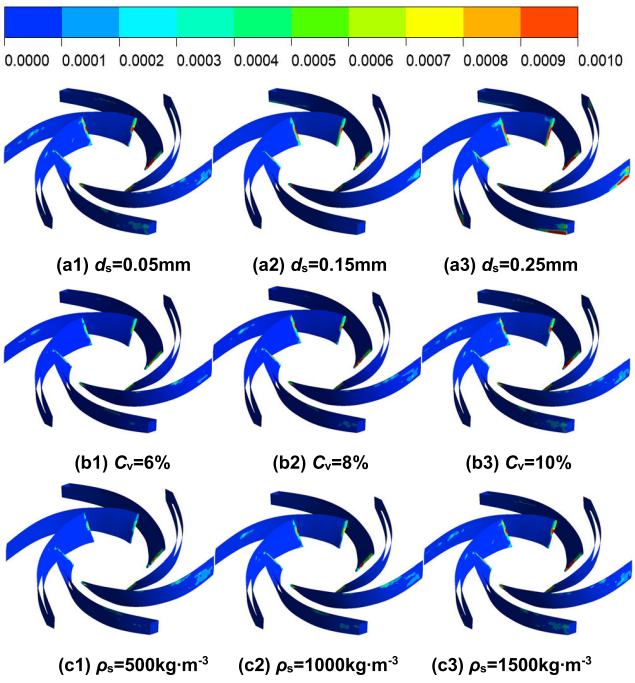

FIGURE 10. Abrasion distribution of blades with different particle properties (a1-a3: particle diameter; b1-b3: solid-phase concentration; c1-c3: particle density).

Fig. 10 shows the wear cloud of the blades for different particle diameters. When the solid-liquid mixture enters the impeller region from the pump inlet, it is firstly subject to the shunt effect of each blade to enter each blade runner, solid particles directly collide with the impact of the blade head, resulting in serious wear and tear in this region. As shown in the figure, the abrasion in the blade head is the most serious for all the different solid phase property conditions. It is also found that the abrasion caused by particle impact on the blade head gets more serious as the solid-phase particle diameter, solid-phase density, and solid-phase concentration increase. When the particle diameter increases from 0.05 mm to 0.25 mm, the area of the serious abrasion in the blade head expands nearly twofold. When the solid-phase concentration increases from 6% to 10%, the maximum abrasion degree of the blade head increases from 0.0008kg/m^{2}s to 0.0010kg/m^{2}s. When the particle density increases from 500 kg· m^{-3} to 1500 kg· m^{-3}, the maximum abrasion degree of the blade head also intensifies from 0.0008 kg/m^{2}s to 0.0010 kg/m^{2}s. It is also found that at a particle diameter of 0.25 mm, serious abrasion occurs at the pressure surface of the blade tail near the hub, with a maximum abrasion degree of about 0.0010 kg/m^{2}s. In contrast, the abrasion in this region is lighter in the case of small particles. Comprehensively, the abrasion of the blade is concentrated in the blade head, and the abrasion degree of the head is more serious with the increase of the solid-phase particle diameter, solid-phase concentration, and solid-phase density. Compared to the abrasion of the blade head, the abrasion of the other blade areas is relatively light.

Fig. 11 shows the wear cloud of the shroud at different solid-phase concentrations. Unlike the abrasion scenario of the volute and blades, as the particle diameter increases, the abrasion of the shroud decreases, and the abrasion area decreases. At a particle diameter of 0.05 mm, there is a certain degree of abrasion throughout the entire shroud, especially in the shroud region near the blade head, where abrasion is most serious, with an abrasion degree of about 0.0005 kg/m^{2}s. In contrast, as the particle diameter increases, the abrasion area of the shroud decreases, and the abrasion degree decreases to only about 0.0003 kg/m^{2}s. At a particle diameter of 0.15 mm, the abrasion of the shroud is mainly concentrated near the blades' pressure surface, accounting for about one-half of the flow channel. At a particle diameter of 0.25 mm, the abrasion of the shroud is also mainly concentrated near the blades' pressure surface, nearly accounting for about one-third of the flow channel. It is evident that the abrasion area decreases with increasing particle diameter for the shroud.

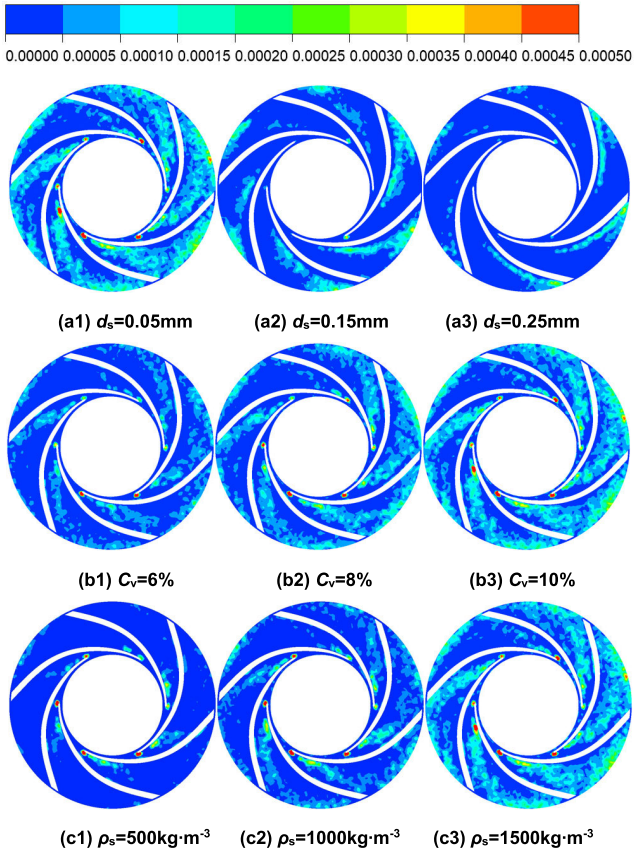

FIGURE 11. Abrasion distribution of shroud with different particle properties (a1-a3: particle diameter; b1-b3: solid-phase concentration; c1-c3: particle density).

Fig. 11b_1-b_3 shows the wear cloud of the shroud at different solid-phase concentrations. At a solid-phase concentration of 6%, the entire shroud region is subjected to some wear, but the abrasion distribution is more disorganized. As the solid-phase concentration increases, the abrasion area of the shroud increases significantly, and the abrasion is

distributed over almost the entire shroud. It was also found that regardless of the solid-phase concentration, the abrasion of the shroud near the blade head is the most serious, about 0.0005 kg/m^{2}s.

Fig. 11c$_1$-c$_3$ shows the wear cloud of the shroud for different solid-phase densities. At a solid-phase density of 500 kg· m^{-3}, the abrasion is mainly concentrated in the shroud region near the blade head, with a maximum abrasion degree of about 0.0005 kg/m^{2}s, and almost no abrasion in other regions. As the solid-phase density increases, the abrasion area of the shroud continues to expand. As can be seen at a solid-phase density of 1500 kg· m^{-3}, the abrasion is distributed over almost the entire shroud, with the worst abrasion remaining in the shroud region near the blade head. In summary, as the particle diameter increases, the abrasion area of the shroud decreases, and the abrasion degree decreases; as the solid-phase concentration and density increase, the abrasion area of the shroud increases, and the abrasion degree increases.

Fig. 12 shows the wear cloud of the hub at different particle diameters. At particle diameters of 0.05 mm and 0.15 mm, there is a certain abrasion in all regions of the hub except for the center region, but the abrasion is distributed in a disordered manner. Moreover, when the particle diameter is 0.25mm, the abrasion distribution shows a certain pattern, and the abrasion of the hub is mainly concentrated near the blades' pressure surface, which accounts for about one-half of the flow channel. It is also found that the worst abrasion of the hub is found both near the head and tail of the pressure surface, with an abrasion degree of about 0.0005 kg/m^{2}s. As seen, the change in particle diameter mainly affects the location of the abrasion distribution of the hub and the abrasion degree, and has less effect on the size of the abrasion area.

Fig. 12b$_1$-b$_3$ shows the wear cloud of the hub at different solid-phase concentrations. It shows that the solid-phase concentration increases, the abrasion area of the hub gets larger and the abrasion at the edges of the hub gets more serious. At a solid-phase concentration of 6%, the abrasion is mainly concentrated in the edge region as well as near the blade in the hub region, and the abrasion near the blade head and in the edge region is more serious with about 0.0003 kg/m^{2}s. And at a solid-phase concentration of 10%, except for the center of the hub, the abrasion in all other regions increases. Significantly, the change of abrasion in the edge region of the hub is the most obvious, and the abrasion region of the edge increases, and the abrasion degree is aggravated, which is about 0.0005kg/m^{2}s.

Fig. 12c$_1$-c$_3$ shows the wear cloud of the hub at different solid-phase densities. As can be seen, when the solid-phase density is 500kg· m^{-3}, the abrasion on the whole hub is extremely light, and the abrasion is only sporadically distributed at the edge of the blade and the edge of the hub, with a maximum abrasion degree of about 0.00015kg/m^{2}s. As the solid-phase density increases, the abrasion of the hub located at the edge of the blade and the edge of the hub increases,

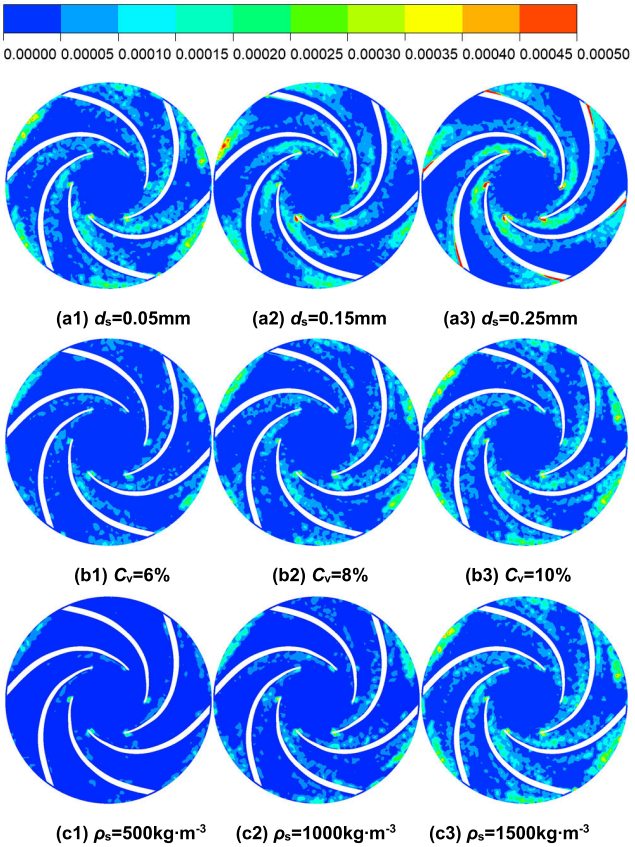

FIGURE 12. Abrasion distribution of hub with different particle properties (a1-a3: particle diameter; b1-b3: solid-phase concentration; c1-c3: particle density).

and the abrasion area increases. At a solid-phase density of 1500 kg· m^{-3}, almost all regions are worn except for the center of the hub, with a maximum abrasion degree of about 0.0005 kg/m^{2}s at the edge of the hub and the edge of the blades.

Fig. 13 shows the particle trajectories for different particle diameters. As can be seen in the figure, the solid particles flow uniformly and at a low velocity of about 4.0 m/s at the inlet. Subsequently, the particles enter the impeller region and move along the blade surface, and the particle flow velocity gradually increases from the impeller inlet to the impeller outlet, with some of the particles reaching a maximum flow velocity of about 20.0 m/s at the end of the blade. Finally, the solid-phase particles enter the volute region and flow out along the volute. It was also found that the particle flow velocity inside the volute decreases, especially the flow velocity of particles near the wall of the volute, which is the smallest, with a minimum flow velocity of about 2.0 m/s.

Compared with the particle flow trajectories at different particle diameters, it can be found that the flow of big particles in the impeller region is closer to the blades' pressure surface. At a particle diameter of 0.05 mm, the particle trajectory is more uniformly distributed in the impeller channel. And as the particle diameter increases to 0.25 mm, the particle

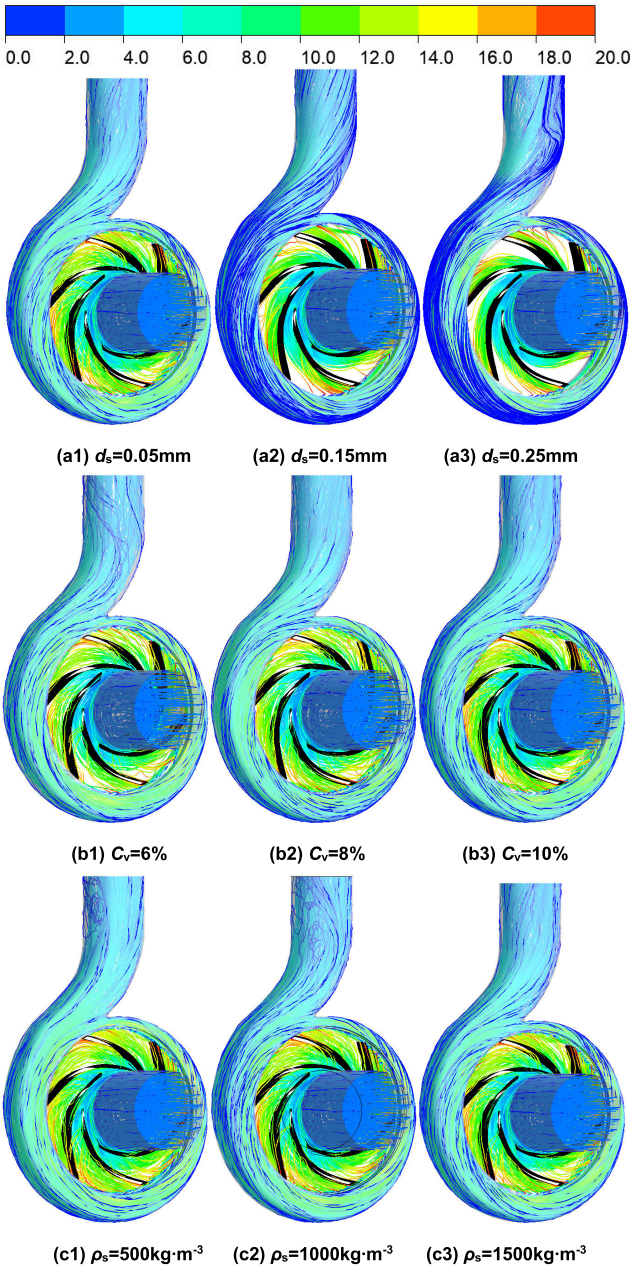

FIGURE 13. Particle trajectories with different particle properties (a1-a3: particle diameter; b1-b3: solid-phase concentration; c1-c3: particle density).

trajectory is gradually denser and closer to the blades' pressure surface, accounting for about one-half of the impeller channel. It is also found that there are fewer low-velocity particles close to the volute wall in small particle conditions and more low-velocity particles close to the volute wall in big particle conditions. That's because small particles can better follow the fluid flow, and small particles are more uniformly distributed within the pump, resulting in more uniform particle trajectories. In contrast, under big particle conditions, the fluid following of the particles is poor, the velocity difference between the solid and liquid phases increases, and the particles are concentrated on one side of the working surface inside the impeller, and then gather on the wall of the volute after leaving the impeller, in agreement with the findings of Huang et al. [46].

Fig. 13b_1-b_3 shows the particle trajectories for different solid-phase concentrations. Due to the particle diameter of different solid-phase concentrations being 0.05mm, the particle diameter is small, so the particles following the fluid performance are better, the particles are more uniformly distributed in the pump, so the difference in particle trajectory under different concentrations is small. It indicates that the particle trajectories are uniformly distributed under different solid-phase concentrations, and the particle trajectories in the impeller region are not densely close to the blades' pressure surface. However, because of the different particle concentrations, the number of particles in the pump is different, resulting in the particle trajectories at low concentrations being sparser than those at high concentrations. Fig. 13c_1-c_3 shows the particle trajectories for different solid-phase densities, and the differences in particle trajectories are quite small. In summary, the particle diameter's size greatly influences the distribution of particles in the pump and the particle trajectory, and the particle concentration and particle density have a smaller influence on the particle trajectory.

IV. DISCUSSION

This paper mainly conducts numerical research on a centrifugal pump with specific speed $n_s = 93$ by using numerical calculation methods to grasp its hydraulic characteristics and abrasion when conveying solid-liquid mixing, which provides a reference for the subsequent optimization and finalization of the pump. However, although the numerical research method has been applied maturely, the accuracy of the calculation results in this paper still needs to be further verified in future work. In addition, this paper only explores the centrifugal pump characteristics when the conveying medium is a mixture of water and particles, and the effects of other different conveying media (such as a mixture of oil and particles) on the hydraulic characteristics and wall wear also need to be explored in future work.

V. CONCLUSION

(1) The pump's hydraulic performance decreases as the solid-phase particle diameter and concentration increase. As the solid-phase density increases, the head and efficiency of the solid-liquid pump tend to increase first and then decrease.

(2) Solid-phase properties affect hydraulic performance to the extent that solid-phase volume fraction > solid-phase density > solid-phase particle diameter.

(3) The abrasion in the volute region is mainly concentrated in the small warp angle region, and the abrasion of the blades is mainly concentrated in the blade head. Except for the shroud, the abrasion of each over-flow component worsens with the increase of solid-phase particle diameter, solid-phase concentration, and solid-phase density. The abrasion at the

shroud decreases as the diameter of the solid phase particles increases.

(4) The hydraulic loss is mainly concentrated in the walls, and the junction region of the impeller and the volute. As the solid-phase volume fraction increases, the hydraulic loss near the blades increases.

REFERENCES

[1] B. Kim, M. H. Siddique, S. A. I. Bellary, A. S. Aljehani, S.-W. Choi, and D.-E. Lee, "Investigation of a centrifugal pump for energy loss due to clearance thickness while pumping different viscosity oils," *Results Eng.*, vol. 18, Jun. 2023, Art. no. 101038, doi: 10.1016/j.rineng.2023.101038.

[2] Y. Wang, L. Zhou, M. Han, and L. Shen, "Performance prediction of an optimized centrifugal pump with high efficiency," *Fluid Dyn. Mater. Process.*, vol. 19, no. 9, pp. 2215–2228, May 2023, doi: 10.32604/fdmp.2023.027188.

[3] B. Cui, C. Zhang, Y. Zhang, and Z. Zhu, "Influence of cutting angle of blade trailing edge on unsteady flow in a centrifugal pump under off-design conditions," *Appl. Sci.*, vol. 10, no. 2, p. 580, Jan. 2020, doi: 10.3390/app10020580.

[4] D. Goodman, J. Stulak, and A. N. Rosenbaum, "Left ventricular assist devices: A historical perspective at the intersection of medicine and engineering," *Artif. Organs*, vol. 46, no. 12, pp. 2343–2360, Aug. 2022, doi: 10.1111/aor.14371.

[5] H. Feng, D. Wang, K. Wang, and M. Zhu, "Simulation studies on the hemodynamics of a centrifugal ventricular assist pump," *Int. J. Fluid Machinery Syst.*, vol. 12, no. 3, pp. 181–188, Sep. 2019, doi: 10.5293/ijfms.2019.12.3.181.

[6] O. Babayigit, M. Ozgoren, M. H. Aksoy, and O. Kocaaslan, "Experimental and CFD investigation of a multistage centrifugal pump including leakages and balance holes," *Desalination Water Treat*, vol. 67, pp. 28–40, Jan. 2017, doi: 10.5004/dwt.2017.20153.

[7] W. Li, Y. Long, L. Ji, H. Li, S. Li, Y. Chen, and Q. Yang, "Effect of circumferential spokes on the rotating stall flow field of mixed-flow pump," *Energy*, vol. 290, Mar. 2024, Art. no. 130260, doi: 10.1016/j.energy.2024.130260.

[8] W. Li, H. Li, M. Liu, L. Ji, R. K. Agarwal, and S. Jin, "Energy dissipation mechanism of tip-leakage cavitation in mixed-flow pump blades," *Phys. Fluids*, vol. 36, no. 1, pp. 015115.1–015115.22, Jan. 2024, doi: 10.1063/5.0183540.

[9] W. Li, W. Pu, L. Ji, M. Liu, Q. Yang, X. He, and R. Agarwal, "Vortex dynamics characteristics in the tip region based on Wray–Agarwal model," *Phys. Fluids*, vol. 36, no. 1, pp. 013337.1–013337.20

[10] O. Kocaaslan, M. Ozgoren, M. H. Aksoy, and O. Babayigit, "Experimental and numerical investigation of coating effect on pump impeller and volute," *J. Appl. Fluid Mech.*, vol. 9, no. 7, pp. 2475–2487, Jul. 2016, doi: 10.18869/acadpub.jafm.68.236.25094.

[11] Z. Wang and Z. Qian, "Effects of concentration and size of silt particles on the performance of a double-suction centrifugal pump," *Energy*, vol. 123, pp. 36–46, Mar. 2017, doi: 10.1016/j.energy.2017.01.142.

[12] R. Tarodiya and B. K. Gandhi, "Numerical simulation of a centrifugal slurry pump handling solid-liquid mixture: Effect of solids on flow field and performance," *Adv. Powder Technol.*, vol. 30, no. 10, pp. 2225–2239, Oct. 2019, doi: 10.1016/j.apt.2019.07.003.

[13] Y. Wang, B. Chen, Y. Zhou, J. Ma, X. Zhang, Z. Zhu, and X. Li, "Numerical simulation of fine particle solid-liquid two-phase flow in a centrifugal pump," *Shock Vibrat.*, vol. 2021, pp. 1–10, Feb. 2021, doi: 10.1155/2021/6631981.

[14] Y. Li, Z. Zhu, W. He, and Z. He, "Numerical simulation and experimental research on the influence of solid-phase characteristics on centrifugal pump performance," *Chin. J. Mech. Eng.*, vol. 25, no. 6, pp. 1184–1189, Oct. 2012, doi: 10.3901/cjme.2012.06.1184.

[15] Y. Zhang, Y. Li, B. Cui, Z. Zhu, and H. Dou, "Numerical simulation and analysis of solid-liquid two-phase flow in centrifugal pump," *Chin. J. Mech. Eng.*, vol. 26, no. 1, pp. 53–60, Jan. 2013, doi: 10.3901/cjme.2013.01.053.

[16] J. H. Liu and M. Y. Zhu, "Numeration simulation of solid-liquid two-phase flow in centrifugal sewerage pump," *Appl. Mech. Mater.*, vols. 44–47, pp. 345–348, Dec. 2010, doi: 10.4028/www.scientific.net/amm.44-47.345.

[17] R. Wang, Y. Guan, X. Jin, Z. Tang, Z. Zhu, and X. Su, "Impact of particle sizes on flow characteristics of slurry pump for deep-sea mining," *Shock Vibrat.*, vol. 2021, pp. 1–13, Mar. 2021, doi: 10.1155/2021/6684944.

[18] W. Zhao and G. Zhao, "Numerical investigation on the transient characteristics of sediment-laden two-phase flow in a centrifugal pump," *J. Mech. Sci. Technol.*, vol. 32, no. 1, pp. 167–176, Jan. 2018, doi: 10.1007/s12206-017-1218-6.

[19] Y. Wang, X. Wang, J. Chen, G. Li, H. Liu, and W. Xiong, "Numerical simulation of the influence of mixed sand on erosion characteristics of centrifugal pump," *Eng. Computations*, vol. 39, no. 6, pp. 2053–2080, Jan. 2022, doi: 10.1108/ec-10-2021-0602.

[20] Y. Li, X. Zeng, W. Lv, and Z. He, "Centrifugal pump wear for solid–liquid two-phase flows based on computational fluid dynamics–discrete element method coupling," *Adv. Mech. Eng.*, vol. 12, no. 7, Jul. 2020, Art. no. 168781402093795, doi: 10.1177/1687814020937951.

[21] S. Hong and X. Hu, "Study on the non-steady-state wear characteristics and test of the flow passage components of deep-sea mining pumps," *Appl. Sci.*, vol. 12, no. 2, p. 782, Jan. 2022, doi: 10.3390/app12020782.

[22] S. Hong and X. Hu, "Research on wear characteristics and experiment on internal through-passage components for a new type of deep-sea mining pump," *Processes*, vol. 10, no. 1, Dec. 2021, Art. no. 58, doi: 10.3390/pr10010058.

[23] G. Peng, X. Huang, L. Zhou, G. Zhou, and H. Zhou, "Solid-liquid two-phase flow and wear analysis in a large-scale centrifugal slurry pump," *Eng. Failure Anal.*, vol. 114, Aug. 2020, Art. no. 104602, doi: 10.1016/j.engfailanal.2020.104602.

[24] Y. X. Liu, R. T. Wang, M. W. Chao, and L. J. Zhang, "Numerical simulation study on erosive wear of ESP," *Chem. Eng. Trans.*, vol. 55, pp. 127–132, Dec. 2016, doi: 0.3303/CET1655022.

[25] Y. A. Khalid and S. M. Sapuan, "Wear analysis of centrifugal slurry pump impellers," *Ind. Lubrication Tribol.*, vol. 59, no. 1, pp. 18–28, Feb. 2007, doi: 10.1108/00368790710723106.

[26] X. Jia, S. Shen, S. Zhang, H. Lv, Z. Lin, and Z. Zhu, "Influence of tip clearance on internal energy loss characteristics of axial flow pumps under different operating conditions," *Phys. Fluids*, vol. 36, no. 1, Jan. 2024, Art. no. 015102, doi: 10.1063/5.0180984.

[27] X. Li, H. Yang, J. Ge, S. Zhu, and Z. Zhu, "Intelligent cavitation recognition of a canned motor pump based on a CEEMDAN-KPCA and PSO-SVM method," *IEEE Sensors J.*, vol. 24, no. 4, pp. 5324–5334, Feb. 2024, doi: 10.1109/JSEN.2023.3347248.

[28] X. J. Li, T. Ouyang, Y. P. Lin, and Z. C. Zhu, "Interstage difference and deterministic decomposition of internal unsteady flow in a five-stage centrifugal pump as turbine," *Phys. Fluids*, vol. 35, no. 4, Apr. 2023, Art. no. 045136, doi: 10.1063/5.0150300.

[29] R.-J. Zhao, Y.-L. Zhao, D.-S. Zhang, Y. Li, and L.-L. Geng, "Numerical investigation of the characteristics of erosion in a centrifugal pump for transporting dilute particle-laden flows," *J. Mar. Sci. Eng.*, vol. 9, no. 9, p. 961, Sep. 2021, doi: 10.3390/jmse9090961.

[30] Y. Yang, H. Wang, C. Wang, L. Zhou, L. Ji, Y. Yang, W. Shi, and R. K. Agarwal, "An entropy efficiency model and its application to energy performance analysis of a multi-stage electric submersible pump," *Energy*, vol. 288, Feb. 2024, Art. no. 129741, doi: 10.1016/j.energy.2023.129741.

[31] H. K. Versteeg and W. Malalasekera, *An Introduction to Computational Fluid Dynamics: The Finite Volume Method*. New York, NY, USA: Pearson Education, 2007.

[32] H. L. Liu, B. B. Lu, M. G. Tan, Y. Wang, and K. Wang, "Numerical simulation on solid-liquid two phase flow in a double channel pump," *JDIME*, vol. 27, no. 5, pp. 297–301, Sep. 2009.

[33] M. Thiruvengadam, Y. Zheng, and J. C. Tien, "DPM simulation in an underground entry: Comparison between particle and species models," *Int. J. Mining Sci. Technol.*, vol. 26, no. 3, pp. 487–494, May 2016, doi: 10.1016/j.ijmst.2016.02.018.

[34] I. M. Hutchings, "Mechanical and metallurgical aspects of the erosion of metals," in *Proc. Corrosion/Erosion Coal Convers. Syst. Mater. Conf.*, 1979, pp. 393–428.

[35] D. V. Kalaga, R. K. Reddy, J. B. Joshi, S. V. Dalvi, and K. Nandkumar, "Liquid phase axial mixing in solid–liquid circulating multistage fluidized bed: CFD modeling and RTD measurements," *Chem. Eng. J.*, vol. 191, pp. 475–490, May 2012, doi: 10.1016/j.cej.2012.02.091.

[36] A. Kilavuz, M. Ozgoren, L. A. Kavurmacioglu, T. Durhasan, F. Sarigiguzel, B. Sahin, H. Akilli, E. Sekeroglu, and B. Yaniktepe, "Flow characteristics comparison of PIV and numerical prediction results for an unmanned underwater vehicle positioned close to the free surface," *Appl. Ocean Res.*, vol. 129, Dec. 2022, Art. no. 103399, doi: 10.1016/j.apor.2022.103399.

[37] F. R. Menter, "Review of the shear-stress transport turbulence model experience from an industrial perspective," *Int. J. Comput. Fluid Dyn.*, vol. 23, no. 4, pp. 305–316, May 2009, doi: 10.1080/10618560902773387.
[38] W. G. Zhao, J. J. Lu, and F. R. Zhao, "Cavitation control of centrifugal pump based on gap jet principle," *J. Zhejiang Univ.*, vol. 54, no. 9, pp. 1785–1794, Sep. 2020, doi: 10.3785/j.issn.1008-973X.2020.09.015.
[39] J. He, Q. Si, W. Sun, J. Liu, S. Miao, X. Wang, P. Wang, and C. Wang, "Study on the energy loss characteristics of ultra-low specific speed PAT under different short blade lengths based on entropy production method," *Energy*, vol. 283, Nov. 2023, Art. no. 129026, doi: 10.1016/j.energy.2023.129026.
[40] D. Li, H. Wang, Y. Qin, L. Han, X. Wei, and D. Qin, "Entropy production analysis of hysteresis characteristic of a pump-turbine model," *Energy Convers. Manage.*, vol. 149, pp. 175–191, Oct. 2017, doi: 10.1016/j.enconman.2017.07.024.
[41] C. Wang, Y. Zhang, Z. Yuan, and K. Ji, "Development and application of the entropy production diagnostic model to the cavitation flow of a pump-turbine in pump mode," *Renew. Energy*, vol. 154, pp. 774–785, Jul. 2020, doi: 10.1016/j.renene.2020.03.065.
[42] J. Huang, J. Gong, L. Wang, H. Affane, Q. Zhang, and J. Zhang, "Optimal design of fluidic diode for valveless piezoelectric pump based on entropy production theory," *Sens. Actuators A, Phys.*, vol. 356, Jun. 2023, Art. no. 114342, doi: 10.1016/j.sna.2023.114342.
[43] F. Kock and H. Herwig, "Local entropy production in turbulent shear flows: A high-Reynolds number model with wall functions," *Int. J. Heat Mass Transf.*, vol. 47, nos. 10–11, pp. 2205–2215, May 2004, doi: 10.1016/j.ijheatmasstransfer.2003.11.025.
[44] W. G. Zhao, Y. J. Zheng, Y. Liu, and X. D. Han, "Numerical analysis of effect of sand volume fractions on erosion characteristics of centrifugal pump," (in Chinese), *JDIME*, vol. 36, no. 2, pp. 98–103, Feb. 2018.
[45] A. A. Noon and M.-H. Kim, "Erosion wear on centrifugal pump casing due to slurry flow," *Wear*, vols. 364–365, pp. 103–111, Oct. 2016, doi: 10.1016/j.wear.2016.07.005.
[46] S. Huang, W. L. Zhou, J. J. Zhou, D. P. He, and T. Y. Peng, "Unsteady numerical simulation on solid-liquid flows and wear in a centrifugal pump based on DPM model," *Hydromechatronics Eng.*, vol. 44, no. 6, pp. 1–15, Mar. 2016, doi: 10.3969/j.issn.1001-3881.2016.06.001.

YINGYU JI was born in Heilongjiang, China, in 1981. She received the bachelor's degree from Jilin Engineering Normal University, Changchun, China, in 2004, and the master's degree in control engineering from Zhejiang University of Technology, Hangzhou, China, in 2011. She is currently a Senior Experimentalist with Quzhou University. Her current research interest includes the numerical simulation of fluid machinery.

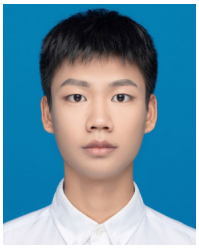

JIANGBO TONG was born in Zhejiang, China, in 2000. He received the bachelor's degree from Quzhou University, Quzhou, China, in 2022. He is currently pursuing the M.S. degree with the Department of Mechanical Engineering, Hunan University of Technology, Zhuzhou, China. His current research interest includes the numerical simulation of fluid machinery.

YULIANG ZHANG was born in Shandong, China, in 1978. He received the Ph.D. degree in mechatronic engineering from Zhejiang University, China, in 2013. He is currently a Professor with Quzhou University. His current research interests include flow control and fluid machinery design.

XIAOWEI XU was born in Henan, China, in 1984. He received the Ph.D. degree in optical engineering from Soochow University, China, in 2014. He is currently an Associate Professor with Quzhou University. His current research interests include digital microfluidics and biochips.

YANJUAN ZHAO was born in Gansu, China, in 1979. She received the master's degree in software engineering from Lanzhou University, China, in 2008. She is currently a Lecturer with Quzhou College of Technology. Her current research interest includes numerical simulation of fluid machinery.

JINSHUN ZHU was born in Zhejiang, China, in 1978. He received the bachelor's degree in power engineering and automation from Gansu University of Technology, China, in 2002. He is currently a Chief Engineer with Visu Autotec (Ningbo) Company Ltd. His current research interest includes energy and power.